Research Square

Preprints are preliminary reports that have not undergone peer review.
They should not be considered conclusive, used to inform clinical practice,
or referenced by the media as validated information.

A handful of co-active synapses is sufficient to drive principal neurons along the hippocampal trisynaptic circuit

Alessandro Fiasconaro
Universidad de Zaragoza
Pierpaolo Arenare
National Research Council
Michele Migliore
National Research Council
Rosanna Migliore
rosanna.migliore@cnr.it

National Research Council

Article

Keywords:

Posted Date: November 24th, 2026

DOI: https://doi.org/10.21203/rs.3.rs-11597553/v1

License: This work is licensed under a Creative Commons Attribution 4.0 International License.
Read Full License

Additional Declarations: No competing interests reported.

A handful of co-active synapses is sufficient to drive principal neurons along the hippocampal trisynaptic circuit

Alessandro Fiasconaro[1,2,3], **Pierpaolo Arenare**[1], **Michele Migliore**[1,4], **and Rosanna Migliore**[1,*]

[1]Institute of Biophysics, National Research Council, Palermo, Italy
[2]Department of Condensed Matter Physics, University of Zaragoza, Zaragoza, Spain
[3]Institute for Biocomputation and Physics of complex Systems, University of Zaragoza, Zaragoza, Spain
[4]European Brain Research Institute-Fondazione Rita Levi-Montalcini, Rome, Italy
[*]Corresponding author: Rosanna Migliore. email: rosanna.migliore@cnr.it

ABSTRACT

How many presynaptic neurons must be co-active to drive a neuron is a basic determinant of its computational properties, yet it cannot be measured directly. We addressed this question for the principal neurons of the hippocampal trisynaptic circuit, using biophysically detailed models with experimentally constrained synaptic number, strength, location, and short-term dynamics. Synchronous activation of only 5–13 perforant-path synapses (2–7 entorhinal neurons), 63–68 mossy-fiber contacts (about two granule cells), and 2–8 Schaffer collateral synapses (1–4 CA3 neurons) was sufficient to drive granule, CA3, and CA1 neurons, less than 5% of the anatomical convergence onto each cell type. The stages also differed in input summation (sublinear, linear, and supralinear) and in how short-term dynamics transformed input rate: depression made granule cells insensitive to afferent rate, facilitation allowed a single repetitively firing granule cell to drive CA3, and balanced dynamics allowed CA1 to follow input rate. Because so few inputs suffice, a single neuron can be driven by an extremely large number of distinct, minimally overlapping groups of afferents, and its selectivity among them can be changed by modifying only a handful of synapses. Hippocampal neurons may thus act as detectors of many small, independent assemblies rather than as integrators of global afferent activity.

1 Introduction

The hippocampus plays a central role in cognitive processes essential for survival, including spatial learning, episodic memory, and contextual association[1–5]. These functions rely on structured activity propagation along the hippocampal trisynaptic circuit, in which cortical inputs from the Entorhinal Cortex (EC) are sequentially processed by Dentate Gyrus (DG), CA3, and CA1 neurons before returning to cortical areas[6–8]. Granule cells in DG and pyramidal neurons in CA3 and CA1 form the main excitatory stages of this pathway, which operates under strong modulation by oscillatory dynamics. Theta rhythms are associated with spatial learning and promote signal propagation and synaptic plasticity within the circuit[9–12], whereas gamma oscillations originating from lateral EC neurons coordinate DG–CA3 interactions during object-related learning[13].

Although anatomical reconstructions and physiological recordings have characterized hippocampal connectivity and oscillatory coordination in detail[6,8,14], a fundamental quantitative issue remains unresolved: how much neuronal and synaptic recruitment is required to ensure reliable transmission of activity across the circuit? A CA1 pyramidal neuron receives more than 10,000 excitatory synapses[15], and a DG granule cell receives several thousand perforant-path contacts[14]. Yet these figures do not specify how many presynaptic neurons must be co-activated, or how many contacts engaged, for activity initiated in EC to reach CA1. Population recordings relate pre- and postsynaptic activity across stages[16], and single-fiber studies show that individual mossy-fiber inputs can be remarkably effective[17,18]. Neither approach, however, reveals the minimal convergence required by each principal cell type.

This quantity is also central to understanding the computational power of individual neurons. Active dendrites and the spatiotemporal arrangement of synaptic inputs allow a single pyramidal cell to perform operations traditionally attributed to networks[19–22]. A CA1 neuron has accordingly been described as a two-layer network[23], and a cortical neuron as a deep multilayer network[24]. A widely held view is that cognitive representations are carried by the cooperative activity of large neuronal assemblies. In an influential formulation[25], Buzsáki defined a cell assembly functionally, by its ability to discharge a downstream "reader" neuron within a single integration window corresponding approximately to one gamma cycle ($\sim$10–30 ms), consistent with the time scale over which peer activity best predicts hippocampal pyramidal cell firing[26]. Within this window,

driving a reader neuron was estimated to require the coordinated activity of tens to hundreds of presynaptic neurons, and therefore the near-simultaneous activation of hundreds of synapses. Quantifying this minimal recruitment for each cell type of the trisynaptic circuit is essential both for predicting whether activity can traverse the pathway and for estimating the computational capacity of its individual neurons: if only a small fraction of a neuron's synapses is sufficient to drive it, the neuron could be driven independently by a large number of small, non-overlapping groups of afferents, increasing the number of distinct input patterns it can detect.

We hypothesize that reliable propagation of activity along the trisynaptic pathway requires the synchronous activation of only a small number of synaptic contacts at each stage, corresponding to a handful of presynaptic neurons. This number would be far below both the anatomical convergence onto each principal cell and the assembly sizes usually assumed to drive a postsynaptic neuron, and would differ across stages, reflecting differences in unitary synaptic strength, dendritic location of inputs, and intrinsic excitability of the postsynaptic cell type. If correct, the identity and timing of a few co-active afferents, rather than the overall level of presynaptic activity, would determine whether a cognitively relevant signal initiated in EC reaches CA1.

To test this hypothesis, we implemented a computational model of the Hippocampal Trisynaptic Circuit (HTC) and systematically analyzed how postsynaptic responses depend on presynaptic firing frequency (4–100 Hz), synaptic conductance, and number of activated synapses. By isolating these variables, the model enables controlled quantification of structural parameters that cannot be independently manipulated *in vivo* or *in vitro*.

While anatomical studies report synapse numbers within the circuit, they do not determine how many are functionally recruited during the transmission of a specific stimulus. An indirect estimate was provided by Bartesaghi et al.[16], who related postsynaptic voltage responses to presynaptic activation levels in the guinea pig trisynaptic pathway. Using their measurements as a physiological reference, we validated our results at each stage of the circuit.

By establishing explicit thresholds for signal transmission, our results provide principled boundary conditions for constructing biologically grounded network models, including sparse coding regimes, gain control mechanisms, and scaling properties of DG–CA3–CA1 circuits. Together, this work links synaptic-scale parameters to circuit-level activation and provides quantitative constraints that bridge cellular dynamics and network computation in the hippocampus.

2 Materials and Methods

2.1 Neuron models

All models were implemented using the NEURON simulation environment[27], and were based on previous works, as indicated below for each neuron. They enabled biophysically grounded simulations capable of reproducing experimentally observed firing dynamics. The specific model files used in this work are available on modelDB (https://modeldb.science/, acc.n. 2041699).

Dentate Gyrus (DG)

The DG granule cell model is based on the revised rat granule cell developed by Ferrante et al.[28]. The original model included Na^+ and K^+ channels distributed uniformly across the membrane. In this work we extended the channel repertoire to reproduce firing responses observed under current clamp conditions[29]. To reproduce the firing properties exhibited by these neurons, we added voltage-dependent Ca^{2+} channels, delayed rectifier potassium channels (KD), M-type potassium channels (KM), and calcium-dependent potassium channels (KC and KAHP). Except for the axon, Ca^{2+} channels were distributed throughout all compartments. Following experimental suggestions, KM channels were localized to soma and axon, while KD channels were restricted to the soma. With this configuration, the model reproduced the experimentally observed linear increase in firing rate with increasing current injection and weak adaptation[29–32], as illustrated in Fig. 1 (DG panels).

CA3 pyramidal neuron

The CA3 pyramidal neuron model is based on Hemond's rat hippocampal CA3 model[33], which incorporates a rich complement of ion channels governing intrinsic excitability. The model includes voltage-gated sodium channels (Na), multiple potassium conductances (KDR delayed rectifier, KA fast inactivating, KD slow inactivating, and KM M-type), calcium-dependent potassium channels (KC and KAHP), voltage-dependent calcium channels (CaN-, L-, and T-type), a hyperpolarization-activated current (IH), and an exponential calcium extrusion mechanism. Channel kinetics follow previously established implementations for CA1 and CA3 pyramidal neurons (NaV, KDR, KA, IH)[34] and (CaV, KM, KC, KAHP)[35–37]. KD conductance and the calcium extrusion mechanism are based on Hemond et al.[33]. All conductances are distributed throughout the neuron unless otherwise specified. KD and KM channels are restricted to the soma. The axon contains Na, KDR, and KA channels, with a fivefold increase in channel density to support reliable axonal action potential initiation. By adjusting channel conductance combinations while preserving morphology, the model reproduces distinct firing phenotypes—bursting, adapting, and non-adapting—shown in Fig. 1 (CA3 panels).

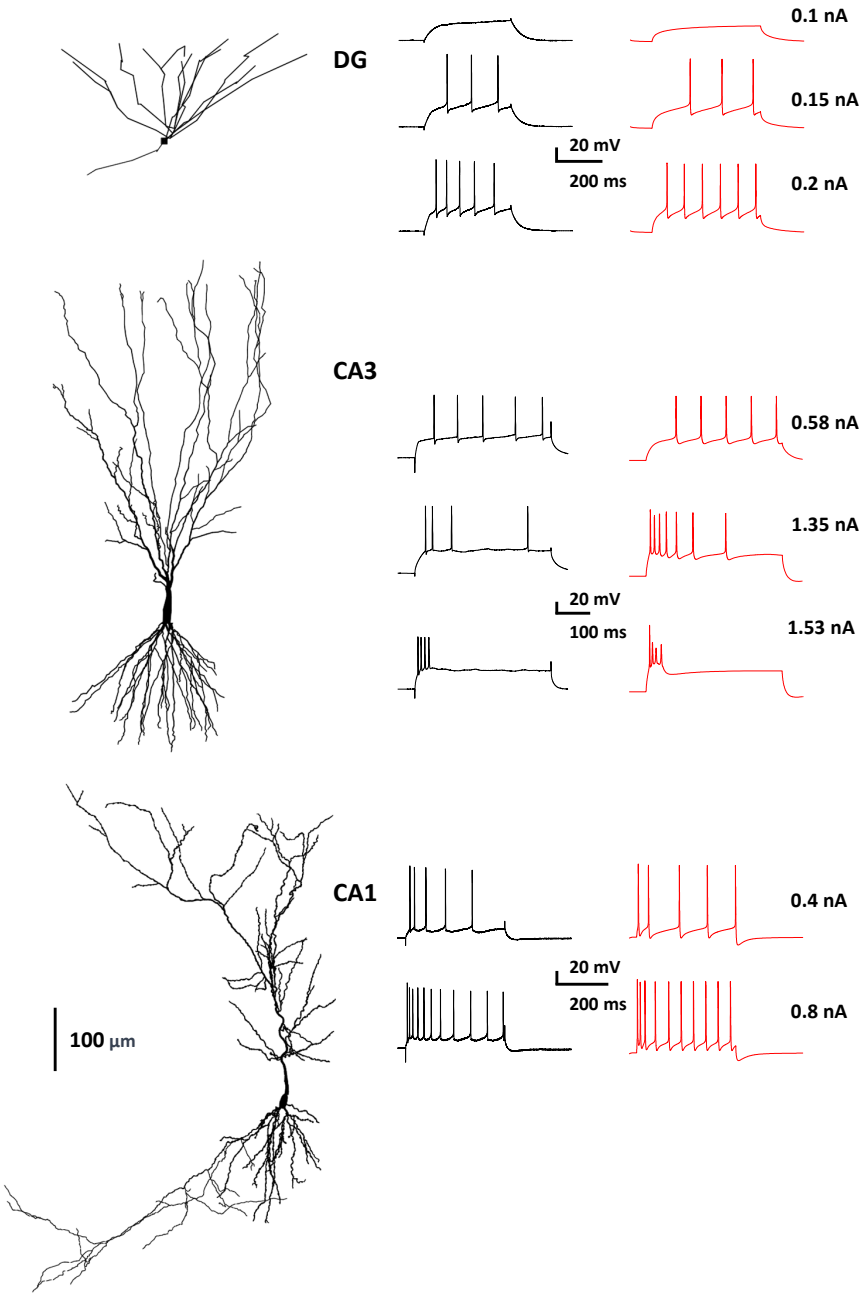


Figure 1. Morphologies of the neurons (DG, CA3, CA1) constituting the Hippocampal Trisynaptic Circuit (HTC) in the model, including soma, axon, and dendritic compartments. On the right-hand side, representative firing traces obtained experimentally (black) and from simulations (red) are shown under constant somatic current injections (indicated on the right of each trace). The three CA3 exp. and model traces correspond respectively to *non-adapting*, *adapting*, and *bursting* firing patterns for three current inputs. In all panels, the experimental traces are from Refs.[29,33,38].

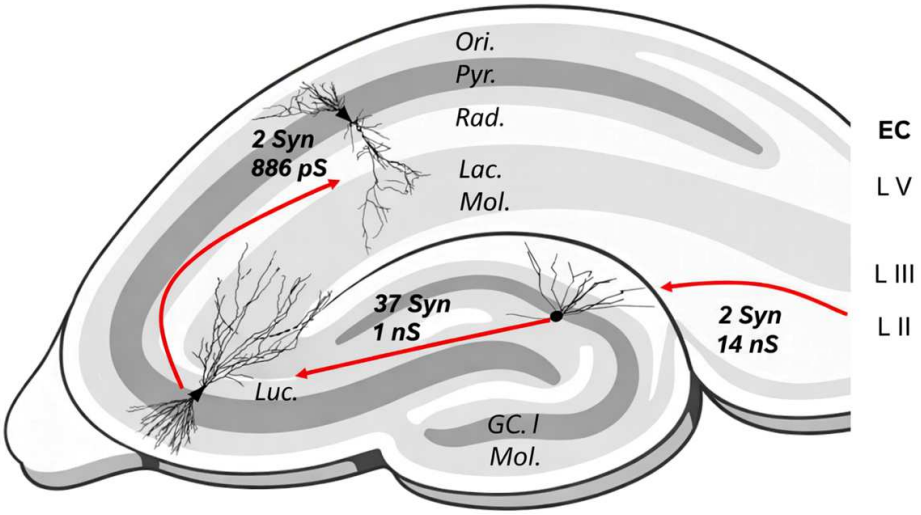


Figure 2. Schematic representation of the Trisynaptic Circuit cytoarchitecture, including the quantitative information on peak synaptic conductances and number of synaptic contacts in the 1:1 configuration used in this work. The EC–DG, DG–CA3, and CA3–CA1 connections are indicated by red arrows; Granule Cell layer (GC.l), Stratum Moleculare (Mol.), Stratum Lucidum (Luc.), Stratum Pyramidale (Pyr.), Stratum Oriens (Ori.), Stratum Radiatum (Rad.), and Stratum Lacunosum Moleculare (Lac. Mol.).

CA1 pyramidal neuron

The CA1 model is a data-driven, multi-compartmental reconstruction optimized using multi-objective genetic algorithms constrained by morphological reconstructions and experimental somatic voltage recordings from rat hippocampal neurons[38,39]. It incorporates the same classes of ion channels as the CA3 model, with differences in maximal conductance values. Dendrites and soma share similar channel distributions, with the exclusive addition of KM channels in the soma. The axon is characterized by voltage-dependent Na and potassium channels (KA, KM, KDR), with densities adjusted to ensure reliable spike initiation and propagation. All compartments include IH conductance and intracellular calcium extrusion mechanisms. An example of the simulated CA1 firing response is shown in Fig. 1 (CA1 panels).

Synaptic transmission

To reproduce the anatomical organization of the circuit, synapses were randomly distributed within physiologically appropriate dendritic regions for each neuron type, following the available experimental evidence (see the following section for details). Briefly, in DG granule cells, synapses were placed at distances greater than 75 μm from the soma, corresponding to the outer three-quarters of the Stratum Moleculare. In CA3 pyramidal neurons, synapses were distributed between 0 and 150 μm from the soma, corresponding to the Stratum Lucidum. In the CA1 model, synapses were located between 0 and 330 μm from the soma, corresponding to the Stratum Radiatum. Short-term synaptic dynamics were implemented using a Tsodyks–Markram-type scheme, with AMPA and NMDA components and parameters chosen to reproduce the experimentally observed facilitation/depression at each synapse type (Supplementary Figures S1-S3).

2.2 Hippocampal Trisynaptic circuit model

The implementation of the Hippocampal Trisynaptic Circuit (HTC) (Fig. 2) refers to quantitative anatomical data from the rodent hippocampus. Signal transmission is analyzed between single presynaptic–postsynaptic neuron pairs at each stage of the pathway. This reduction does not aim to replicate the full anatomical convergence and divergence of the rat hippocampal network. Instead, it provides a controlled framework to quantify the minimal synaptic and neuronal recruitment required for deterministic signal propagation. By preserving realistic synaptic multiplicity per connection while isolating individual neuron pairs, the model allows derivation of transmission thresholds that can subsequently be scaled to mesoscopic and large-scale network simulations or to constrain the computational power of a given neuron type. For each stage, the number of synapses, their dendritic location, and their peak conductance are derived from experimental findings and are summarized in Table 1.

At the first stage of the HTC, a DG granule cell receives inputs from layer II neurons of the Entorhinal Cortex (EC). Experimental estimates indicate that each DG granule cell receives up to 8,630 excitatory synapses from approximately 3,542 EC neurons in the rat[14], thus suggesting that each EC neuron makes approximately two synapses with any given DG granule cell. In the model, two EC synaptic contacts are placed onto the outer three-quarters of the Stratum Moleculare dendrites[40,41],

Table 1. Number, peak conductance, and dendritic location of individual synaptic inputs on a given principal neuron type. Superscripts indicate the corresponding experimental references.

	DG	CA3	CA1
Nr. synapses	2	37	2
Conductance	14 nS[42]	1 nS[17]	0.886 nS[43]
Distribution (from soma)	>75 μm	[0,150] μm	[0,330] μm

consistent with rat anatomical descriptions[8,14].

The DG axon projects to CA3 pyramidal neurons via mossy fibers terminating in the Stratum Lucidum[8]. In the rat, a single DG granule cell forms multiple synaptic contacts onto an individual CA3 pyramidal neuron, with approximately 46 DG neurons contacting any given CA3 neuron[14]. Following experimental indications[8], in the model this projection is represented by 37 synaptic contacts onto the CA3 neuron, preserving the strong, multi-contact nature of mossy fiber transmission.

The final stage corresponds to the CA3–CA1 projection mediated by Schaffer collaterals. In the rat hippocampus, CA3 axons target CA1 pyramidal dendrites primarily within Stratum Radiatum and Stratum Oriens. Quantitative analyses report that a CA1 pyramidal neuron receives approximately 12,104 Schaffer collateral synapses[44], originating from around 5,500 CA3 pyramidal neurons[14], corresponding to an average of approximately 2 synapses per individual CA3–CA1 pair.

This reduced framework is motivated by the need to isolate quantities that are difficult to access both experimentally and in large-scale simulations. Experimentally, the number of synapses that must be co-activated to drive a postsynaptic neuron cannot easily be measured. Extracellular stimulation recruits an unknown number of afferent fibers, and population recordings quantify the fraction of active neurons rather than the number of contributing synapses[16]. Paired recordings between connected neurons are low-yield and, in slices, are limited by axonal truncation. Glutamate uncaging and single-cell stimulation provide precise control over a few inputs[22], but not over the spatially distributed activation that occurs under physiological conditions. In full-network simulations, the same quantity is obscured by probabilistic connectivity rules and by the simultaneous interaction of thousands of neurons. Analyzing transmission between single presynaptic–postsynaptic pairs, while preserving realistic synaptic multiplicity, strength, and dendritic location, makes it possible to control the number of activated contacts directly and to estimate the minimal recruitment required at each stage.

These estimates bear directly on the computational properties of individual neurons. The ratio between the number of synapses a neuron receives and the number required to make it fire determines how many distinct input combinations it can in principle discriminate. It also determines whether the neuron behaves as a detector of sparse, synchronous input patterns or as an integrator of global afferent activity. The same numbers provide quantitative constraints for network models of pattern separation in DG, pattern completion in CA3, and output integration in CA1. They help ensure that such models operate in biologically plausible regimes of synaptic convergence without replacing them.

3 Results

3.1 Input–output relationship as a function of input frequency and peak synaptic conductance

Granule cells are driven by a few co-active perforant-path inputs, largely independently of input rate. The transfer properties of dentate gyrus granule cells were first characterized by estimating the probability that a neuron generates at least one action potential following a single synchronous activation of a given number of EC synapses (Fig. 3A). The probability was calculated from 100 simulations in which synaptic locations were randomly redistributed within the physiologically relevant dendritic region. The resulting activation curves exhibit a sigmoidal shape, revealing a gradual transition between subthreshold and suprathreshold regimes. As expected, synaptic strength shifted the activation curve along the recruitment axis. The half-activation point (c*) decreased from 14.0 synapses at 7 nS to 9.1 at the physiological value of 14 nS, and to 6.4 at 28 nS. At 14 nS, firing probability rose from 10% to 90% between approximately 5 and 13 activated synapses. The shift, however, was less than proportional to the change in conductance. Halving the peak conductance increased c* by only ∼50%, and doubling it reduced c* by ∼30%. As a result, the total synaptic conductance required for 50% activation probability (∼98, 127, and 179 nS at 7, 14, and 28 nS, respectively) increased with unitary strength. For a given total synaptic drive, therefore, a larger number of weaker inputs was more effective than a few strong ones, consistent with sublinear summation of large local depolarizations. The sigmoidal shape of the activation curve was preserved across conductances, although the transition became somewhat broader for weaker synapses.

The contour plot in Fig. 3B shows the combined effects of synaptic recruitment and presynaptic activation frequency on the postsynaptic firing rate at the physiological conductance. Iso-frequency contours run approximately parallel to the frequency

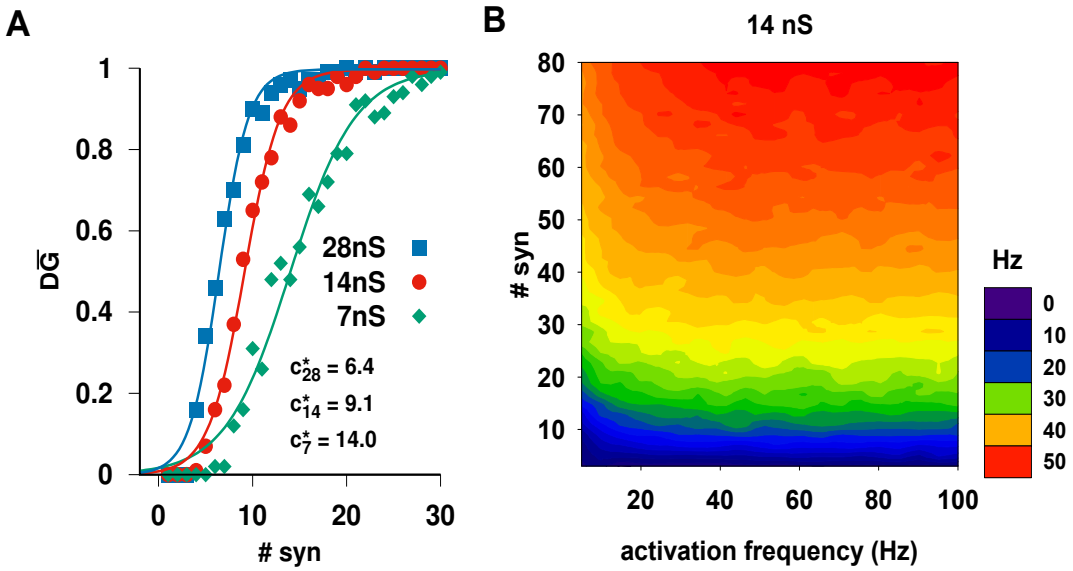


Figure 3. Spike probability of the DG neuron (A) and average output frequency as a function of the number of synapses and their activation frequency, at the nominal value of g_{syn} = 14 nS (B). Solid lines in panel A represent sigmoidal fits, with indicated half value c*.

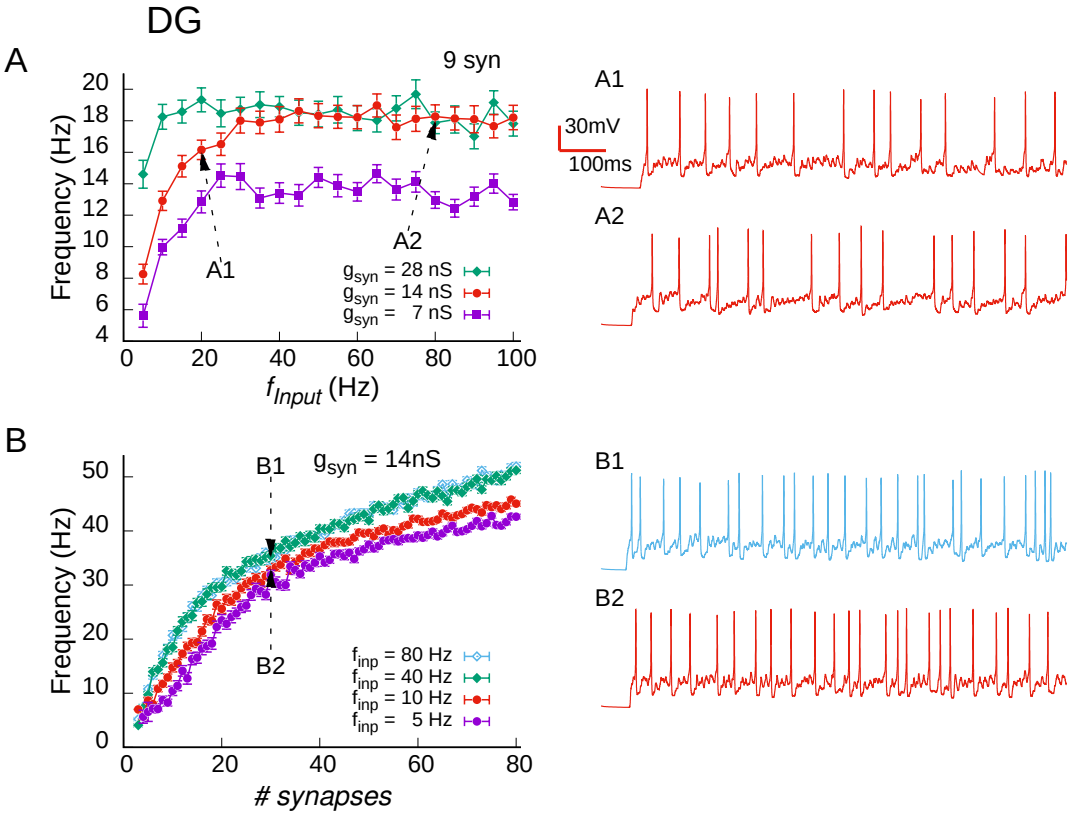


Figure 4. Response of the DG cell. (A) Output frequency as a function of input frequency, with 9 synchronously activated synapses and peak synaptic conductances g_{syn} = 7, 14, and 28 nS. A1 and A2: representative traces at the points indicated. (B) Output frequency as a function of the number of activated synapses for input frequencies of 5, 10, 40, and 80 Hz at the physiological conductance (g_{syn} = 14 nS). Output increases monotonically with the number of synapses. B1 and B2: representative traces at the points indicated.

axis. Over the range tested (20–100 Hz), the output firing rate was therefore determined mainly by the number of activated synapses and changed little with input frequency. This insensitivity largely reflects the short-term depression of perforant-path synapses included in the model (Methods; Supplementary Fig. S1), the efficacy of each synaptic event decreasing almost as fast as the number of events increased. Because depression acts independently at each contact, it limits the drive that can be gained by increasing input frequency, but not the drive gained by recruiting more synapses, which grows in proportion to their number. The effectiveness of EC→DG transmission is therefore determined primarily by the degree of convergent synaptic recruitment rather than by the firing rate of individual afferents.

To separate these contributions, we analyzed the effects of stimulation frequency and synaptic recruitment separately (Fig. 4). In Fig. 4A, the number of activated synapses was fixed at 9, corresponding to ∼50% activation probability at the physiological conductance (c* = 9.1; Fig. 3A). For all conductance values, output firing increased rapidly at low stimulation frequencies and then reached a plateau. At 14 nS, output saturated at ∼18 Hz for inputs above 20–30 Hz, the same range over which the depression-limited synaptic drive approaches its maximum. Increasing the conductance to 28 nS produced only a modest increase in the plateau, whereas reducing it to 7 nS lowered the overall response. The representative voltage traces (Fig. 4A1–A2) show that, once the plateau is reached, large increases in presynaptic frequency produce only small changes in the firing pattern, because each additional input event is progressively weaker. In Fig. 4B, the conductance was fixed at the physiological value and the number of activated synapses was progressively increased. Recruitment then modulated output firing far more than stimulation frequency, and the curves obtained for inputs between 5 and 80 Hz remained close to each other. At all frequencies, the response increased monotonically with recruitment, with the steepest rise within the first 20–30 contacts followed by a gradual saturation. Since short-term depression does not depend on the number of active synapses, this saturation reflects postsynaptic integration, consistent with the sublinear summation observed in Fig. 3A. The representative traces (Fig. 4B1–B2) show that recruiting additional synapses increases spike density much more effectively than increasing presynaptic frequency.

Taken together, these results suggest that DG granule cells are considerably more sensitive to the number of convergent synaptic inputs than to the firing frequency of individual afferents. This observation is particularly noteworthy in light of the anatomical organization of the perforant path. Although each granule cell receives thousands of excitatory synapses from entorhinal cortex neurons[8,14], reliable activation can be achieved through the coordinated recruitment of only about 5-13 synapses, corresponding to a small number of presynaptic EC neurons (Table 2). In our simulations, increasing presynaptic frequency above ∼20–30 Hz produced only limited additional increases in DG output, because short-term depression reduced the efficacy of each additional input event. At theta frequencies, in contrast, each event retained most of its efficacy (∼55–75% of the first response at 5–10 Hz). This may help explain why theta-frequency activity is particularly effective in driving signal propagation through the trisynaptic pathway[9,10]. At these frequencies, each entorhinal spike is transmitted with high efficacy, and repeated volleys can synchronize convergent inputs within temporal windows that efficiently recruit granule cells. More generally, short-term depression acts as a gain-control mechanism that makes the postsynaptic response largely independent of afferent firing rate[45,46]. This leaves the number of co-active inputs as the main determinant of DG output.

The results are also consistent with theoretical frameworks in which the dentate gyrus acts as a filtering and sparsifying stage between entorhinal cortex and CA3, by transforming dense, overlapping cortical input patterns into sparse and more distinct granule cell representations[12,47–52]. Filtering follows from the insensitivity of DG output to input frequency. Because of short-term depression at perforant-path synapses, increases in the firing rate of EC afferents above ∼20–30 Hz produce little additional granule cell output. Sustained or intense cortical activity is therefore not transmitted proportionally to CA3. Sparsification follows from the dependence of DG output on the number of coincident inputs. A granule cell fires only when a sufficient number of its EC afferents, ∼9 synapses or 4–5 EC neurons at half-activation, are active within the same short time window. Because each granule cell samples a different subset of the entorhinal population, only the few cells that happen to receive enough coincident input from a given pattern will fire. At the network level, feedforward and feedback inhibition, which are not included in the present model, are expected to further sharpen both effects[28].

Mossy-fiber input gates CA3 activation through one or two granule cells. The activation properties of adapting CA3 pyramidal neurons (which make up approximately 80% of the CA3 pyramidal neuron population[33]) were first characterized by estimating the probability of generating at least one action potential following the synchronous activation of an increasing number of mossy fiber synapses (Fig. 5A). As for the non-adapting and bursting subtypes (Supplementary Fig. S6), the activation curves showed a sharp sigmoidal transition between silent and active states. For adapting neurons at the physiological conductance (1 nS), firing probability rose from 10% to 90% between approximately 65 and 68 activated synapses, with half-activation at c* = 66.2; the range extended to 63–68 synapses when the bursting and non-adapting phenotypes were included (Supplementary Table ST1). Changing synaptic strength shifted the curve along the recruitment axis without altering its steepness: c* was 33.2 at 2 nS and 132.6 at 0.5 nS. Unlike in DG, this shift was almost exactly inversely proportional to the unitary conductance. The total mossy-fiber conductance required for 50% spike probability was therefore essentially constant (∼ 66 nS) across the three peak synaptic conductances tested (Fig. 5A), indicating near-linear summation of these proximal

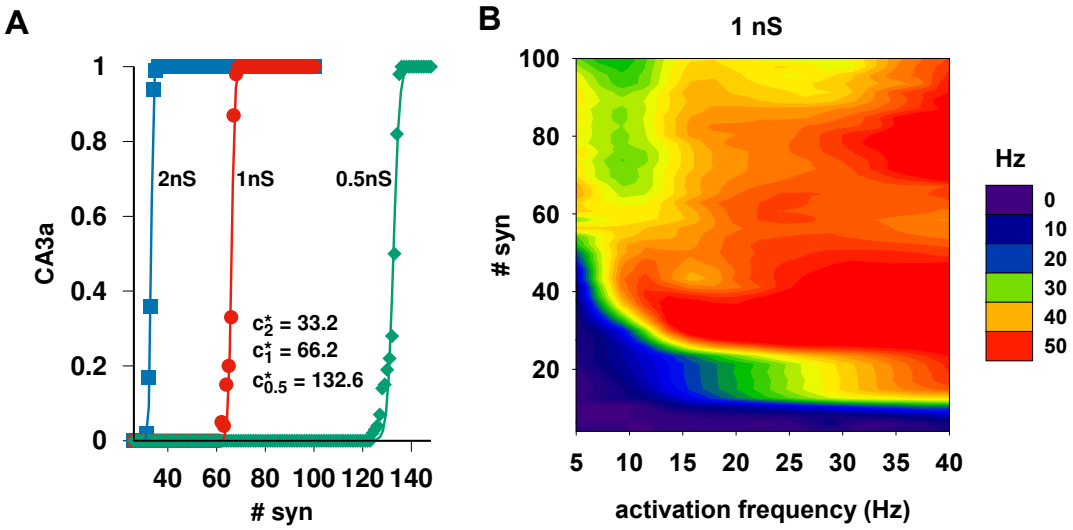


Figure 5. Spike probability of the adapting CA3 neuron (A) and average output frequency as a function of the number of synapses and their activation frequency, at the nominal value of $g_{syn} = 1$ nS (B). Solid lines in panel A represent sigmoidal fits, with indicated half value c*.

inputs. The transition was also far sharper than in DG. Even when the three firing phenotypes were considered together (63–68 synapses), it spanned at most ∼ 8% of c*, compared with roughly the full value of c* in granule cells, and corresponded to fewer contacts than a single granule cell provides (∼ 37; Table 1). At the level of presynaptic neurons, CA3 activation was therefore effectively all-or-none: the input from one granule cell was insufficient, whereas two reliably triggered firing. This behavior is consistent with mossy-fiber transmission acting as a highly selective gate for CA3 activation.

The contour map in Fig. 5B shows the combined effects of synaptic recruitment and presynaptic activation frequency at the physiological conductance. At low recruitment levels, the neuron remained largely silent regardless of stimulation frequency. Once a critical number of synapses was activated, the output firing frequency increased abruptly, reaching values close to 50 Hz. Unlike in DG, this critical level decreased markedly with increasing presynaptic frequency. This frequency dependence reflects the strong short-term facilitation of mossy-fiber synapses included in the model (Methods; Supplementary Fig. S2). Because of their low initial release probability and slowly decaying facilitation, the steady-state efficacy of each synaptic event increased with input frequency, and temporal summation of successive events contributes further to lowering the threshold. At high recruitment and high frequency, the map also contains regions of reduced firing embedded within otherwise highly active regimes. These correspond to combinations in which the total facilitated drive exceeds the optimal range described below and drives the neuron into prolonged depolarization.

To dissect these effects further, we examined the dependence of the output firing frequency on stimulation frequency and on synaptic recruitment separately (Fig. 6). In Fig. 6A, the number of activated synapses was fixed at 66, corresponding to half-activation at the physiological conductance for a single synchronous volley (c* = 66.2; Fig. 5A). In all conditions, the output firing rate exceeded the input frequency, often by several-fold, so that each successful input event triggered multiple spikes rather than a single one. This is expected from facilitation: already at 5 Hz, once facilitation has built up, each synchronous volley produces a synaptic conductance about three times larger than the first volley of the train. The 66 facilitated synapses therefore deliver a drive well above the single-volley threshold. The dependence on input frequency differed markedly between conductances. At 1 nS, output remained relatively flat (∼ 40–50 Hz) over the whole range tested, but the firing pattern changed with frequency. At low input frequency (Fig. 6A1, 10 Hz), successive input events evoked short bursts of spikes separated by pauses. At high input frequency (Fig. 6A2, 40 Hz), the neuron entered a sustained depolarization on which only low-amplitude spikes persisted. Increasing input frequency at this conductance thus raised the facilitated drive beyond the level that the neuron could convert into additional full spikes. At 0.5 nS, output rose steeply at low frequencies and then plateaued at ∼65 Hz, above the values obtained at 1 nS. This apparently paradoxical result follows from the non-monotonic dependence on synaptic drive, discussed in the next paragraph. At 2 nS, output increased approximately linearly with input frequency over the range tested (5–40 Hz). The same inversion between 0.5 and 1 nS was observed in the bursting subtype but not in the non-adapting one (Supplementary Figs. S4A and S5A).

A more striking behavior emerged when conductance was fixed at the physiological value and the number of activated synapses was progressively increased (Fig. 6B). For all input frequencies, firing rose abruptly once a critical recruitment level

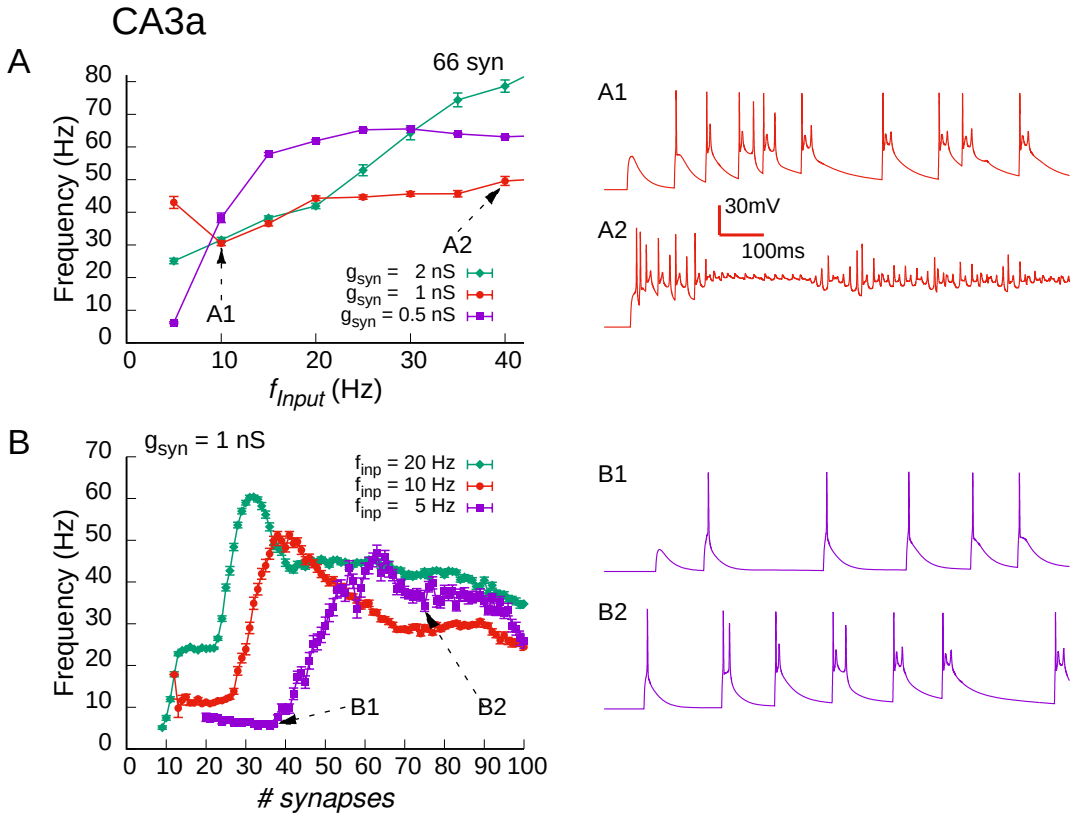


Figure 6. Response of the adapting CA3 pyramidal neuron. (A) Output frequency as a function of input frequency f_{inp}, with 66 synchronously activated mossy-fiber synapses and $g_{\mathrm{syn}} = 0.5$, 1, and 2 nS. At the physiological conductance (1 nS), output varies little with input frequency, with a shallow minimum at 10 Hz. A1 and A2: representative traces at 10 and 40 Hz ($g_{\mathrm{syn}} = 1$ nS). (B) Output frequency as a function of the number of activated synapses for input frequencies of 5, 10, and 20 Hz at $g_{\mathrm{syn}} = 1$ nS. Output is non-monotonic, peaking at a number of synapses that depends on input frequency and declining with further recruitment. B1 and B2: representative traces at the points indicated.

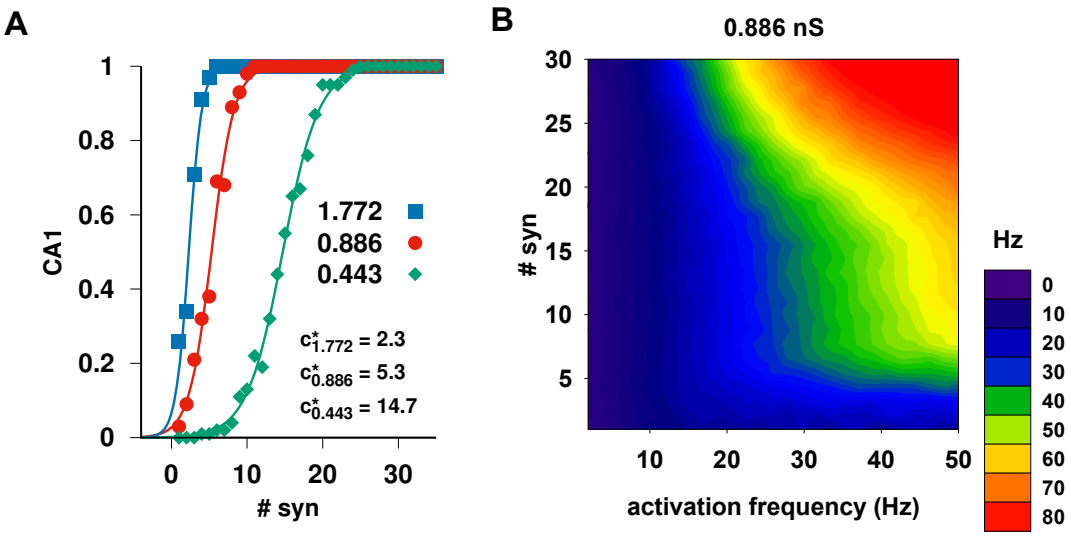


Figure 7. Spike probability of the CA1 neuron (A) and average output frequency as a function of the number of synapses and their activation frequency, at the nominal value of $g_{syn} = 0.886$ nS (B). Solid lines in panel A represent sigmoidal fits, with indicated half value c*.

was reached. This level decreased markedly with input frequency, from ∼ 45 synapses at 5 Hz to ∼ 30 at 10 Hz and ∼ 20 at 20 Hz. All three values are well below the 66 synapses required for half-activation by a single synchronous volley. At 10–20 Hz, they are also below the∼ 37 contacts provided by a single granule cell. Facilitation is sufficient to account for this reduction: with a steady-state efficacy ∼ 4 times that of the first event, the equivalent single-volley threshold falls to ∼ 17 synapses. The observed thresholds are somewhat higher than this estimate, particularly at 5 Hz, because facilitation builds up over several events and output was averaged over the entire stimulation period. Input frequency therefore had a strong effect on the recruitment threshold, the opposite of what was observed in DG. Above threshold, firing peaked at ∼ 50–65 Hz and then declined as additional synapses were recruited. At 10–20 Hz, maximal firing occurred with ∼ 30–50 active synapses, and firing fell to roughly half its peak value at 90–100 synapses. The voltage traces (Fig. 6B1–B2) indicate that this decline is associated with burst discharges, prolonged depolarizations, and periods of reduced excitability that limit sustained spike generation. Because facilitation increases the effective drive of each synapse with frequency, this optimal range is reached with fewer synapses at higher input frequencies. The results for the *adapting* neuron were representative of the other two CA3 subtypes (Supplementary Figs. S4–S6).

Taken together, these results indicate that CA3 pyramidal neurons transform mossy-fiber input in two distinct steps. First, access to firing is governed by a sharp recruitment threshold that is set by the number and strength of mossy-fiber contacts, independently of the intrinsic firing phenotype. For a single synchronous volley, this threshold corresponds to the coincident activity of two granule cells, consistent with the classical view of mossy fibers as "detonator" synapses[17,18]. With repeated activation, however, the threshold falls to ∼20–30 synapses at 10–20 Hz, below the ∼37 contacts provided by a single granule cell. This reduction reflects mainly the pronounced short-term facilitation of mossy-fiber synapses[53,54], which increases the efficacy of each event about fourfold at these frequencies. A single granule cell firing repetitively could therefore discharge its CA3 targets, in line with in vivo observations[18]. The two types of synapse thus have opposite short-term dynamics, which produce complementary transfer properties. Depression at EC–DG synapses makes granule cell output largely insensitive to afferent firing rate, so that DG responds mainly to the number of co-active inputs. Facilitation at mossy-fiber synapses makes CA3 highly sensitive to the firing rate of individual granule cells. As a result, DG can signal to CA3 not only through which granule cells are active but also through how many spikes each one fires.

CA1 neurons follow the rate of a few co-active CA3 inputs. The activation properties of CA1 pyramidal neurons were first characterized by estimating the probability of generating at least one action potential following the synchronous activation of an increasing number of Schaffer collateral synapses (Fig. 7A). As in DG and CA3, the activation curves were sigmoidal, but they were shifted toward much smaller numbers of synaptic contacts. At the physiological conductance (0.886 nS), half-activation occurred at c* = 5.3 synapses, and firing probability rose from 10% to 90% between approximately 2 and 8 activated contacts. This range corresponds to the input from only about 1–4 CA3 neurons (Table 2). Relative to its midpoint, the transition was broad, comparable to that of DG and much wider than the near all-or-none transition of CA3. CA1 activation probability therefore varied gradually with the number of co-active presynaptic neurons.

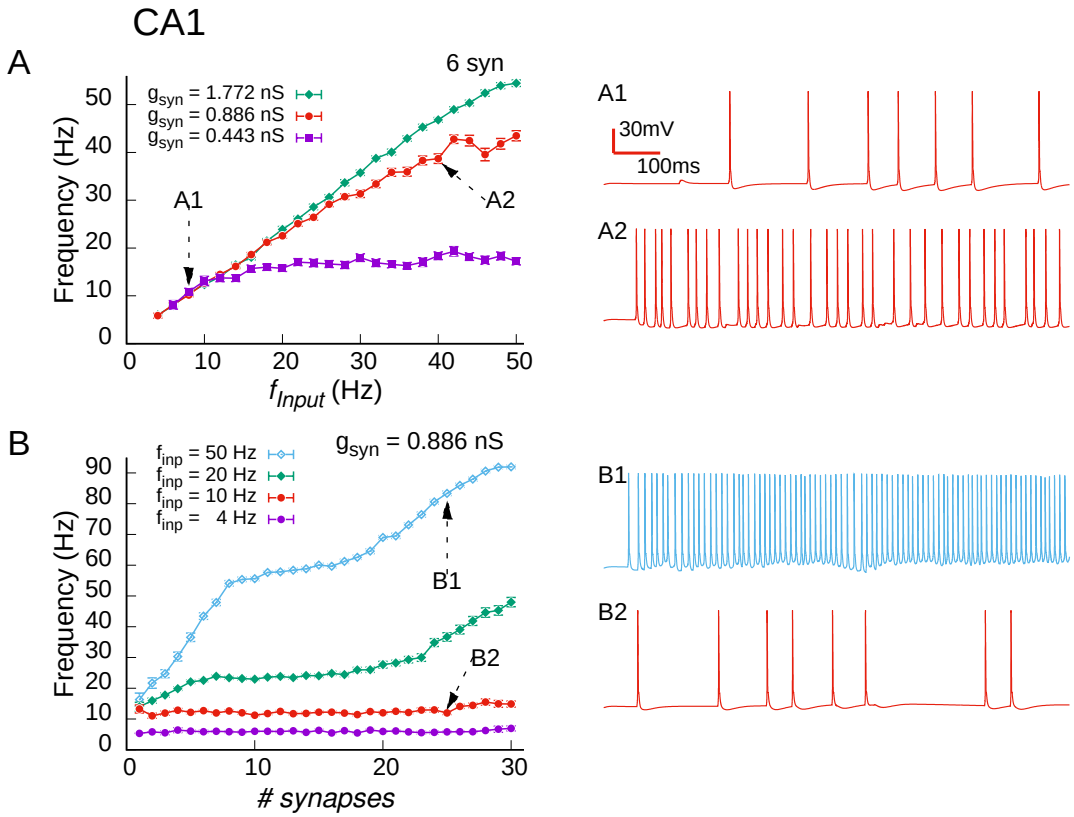


Figure 8. Response of the CA1 pyramidal neuron. (A) Output frequency as a function of input frequency f_{inp}, with 6 synchronously activated Schaffer collateral synapses and g_{syn} = 0.443, 0.886, and 1.772 nS. At the physiological conductance, output increases approximately linearly, with about one spike per input event; with the weakest synapses it saturates at ∼15 Hz. A1 and A2: representative traces at the points indicated. (B) Output frequency as a function of the number of activated synapses for input frequencies of 4, 10, 20, and 50 Hz at g_{syn} = 0.886 nS. At 4 and 10 Hz, output matches the input frequency regardless of the number of synapses; at 20 and 50 Hz, it increases with recruitment in a step-like manner, with a broad intermediate plateau. B1 and B2: representative traces at the points indicated.

Changing synaptic strength shifted the curve along the recruitment axis, with c* = 2.3 at 1.772 nS and 14.7 at 0.443 nS. In contrast to both DG and CA3, however, the shift was more than proportional to the change in conductance: halving the conductance nearly tripled c*, whereas doubling it reduced c* by more than half. The total synaptic conductance required for half-activation therefore increased as unitary strength decreased (∼ 4.1, 4.7, and 6.5 nS at 1.772, 0.886, and 0.443 nS, respectively). In CA1, a few strong inputs were thus more effective than many weak ones, the opposite of the behavior observed in DG. This is consistent with the larger local depolarizations produced by stronger inputs recruiting dendritic regenerative events[21,22].

The contour map in Fig. 7B shows the combined effects of synaptic recruitment and presynaptic activation frequency at the physiological conductance. In contrast to the sharp boundary observed in CA3, iso-frequency contours run diagonally across the map, with a smooth, continuous transition from low- to high-activity regimes. Increasing either stimulation frequency or the number of activated synapses enhanced the postsynaptic response, with output rates reaching ∼ 80 Hz at the highest values of both. This behavior is consistent with the short-term dynamics of Schaffer collateral synapses in the model (Methods; Supplementary Fig. S3). Perforant-path synapses depress, and mossy-fiber synapses facilitate strongly. Schaffer collateral synapses, instead, combine moderate facilitation with depression: relative to the first event, their steady-state efficacy remained within ∼ 1.3–1.5 between 4 and 20 Hz and returned to ∼ 1 at 50 Hz. The drive delivered per unit time by each contact therefore increased almost in proportion to input frequency over most of the range tested. Additional synapses and additional input events thus contribute comparably to the total drive, so that iso-frequency contours follow combinations of recruitment and frequency that deliver similar drive. In DG, synaptic recruitment dominated over stimulation frequency, and in CA3 recruitment beyond an optimal range reduced firing. The CA1 response, by contrast, remained sensitive to both variables and increased monotonically over the entire range explored.

To further characterize these transfer properties, we examined the effects of stimulation frequency and synaptic recruitment separately (Fig. 8). In Fig. 8A, the number of activated synapses was fixed at six, close to half-activation at the physiological conductance for a single synchronous volley (c* = 5.3; Fig. 7A), while stimulation frequency and synaptic conductance were varied. At 0.886 nS, output firing increased almost linearly with input frequency over the entire range tested (up to 50 Hz), with a slope close to one. The neuron thus fired approximately one spike per input event, without the saturation observed in DG or the burst amplification observed in CA3. This follows from the moderate facilitation of Schaffer collateral synapses. Once facilitation has built up, each synchronous volley of six synapses produces a conductance ∼1.3–1.5 times larger than the first. That is equivalent to ∼ 8–9 synapses in a single volley, close to the 90% activation point in Fig. 7A. Nearly every input event therefore elicits a spike, while the drive remains too weak to evoke bursts. Doubling the conductance produced only a modest further increase, with output slightly exceeding the input frequency (∼ 50 Hz at 50 Hz input). Halving it, in contrast, limited the output to ∼ 15 Hz regardless of input frequency. Even with facilitation, six synapses at 0.443 nS remain well below the single-volley threshold at this conductance (c* = 14.7). This residual firing therefore reflects temporal summation of successive events. The representative traces (Fig. 8A1–A2) show that higher frequencies increase spike density while preserving a regular firing pattern.

Fig. 8B shows the dependence of output firing on synaptic recruitment at the physiological conductance. At low stimulation frequencies (4 and 10 Hz), output was essentially independent of the number of activated synapses and matched the input frequency: once threshold was reached, each input event evoked a single spike, and additional recruitment did not add spikes. At higher frequencies, recruitment had a much larger effect. At 20 Hz, output rose from approximately the input frequency to ∼ 45 Hz as the number of synapses increased to 30. At 50 Hz, it rose from ∼ 50 to 90 Hz, with a first step at ∼ 5 synapses and a second, steeper increase above ∼ 20. At these frequencies, intervals between input events (20–50 ms) are short enough for successive synaptic responses to overlap, and the resulting sustained depolarization allows additional spikes between input events. The response never decreased with recruitment. Unlike DG, where output saturated, and CA3, where it was non-monotonic, CA1 therefore maintained a substantial dynamic range over the entire interval examined. The representative traces (Fig. 8B1–B2) illustrate the transition from about one spike per input event to sustained high-frequency discharge as recruitment increases. These results indicate that CA1 neurons operate in a regime distinct from both DG and CA3.

The number of synaptic contacts able to elicit at least one action potential, at each stage, following a synchronous activation with a 10-90% probability is summarized in Table 2. Taken together, these results point to the specific roles of the different neuron populations: DG neurons act as filters of convergent cortical input whose output saturates with input frequency. CA3 neurons act as thresholded amplifiers that convert each suprathreshold event into a burst. CA1 neurons, instead, transmit presynaptic activity with approximately unit gain. At theta-range frequencies, their output follows the input rate faithfully, regardless of how many synapses beyond threshold are recruited. At higher frequencies, additional recruitment increases the number of spikes per input event. This behavior depends in part on the short-term dynamics of Schaffer collateral synapses, whose balance of facilitation and depression makes the drive per contact increase roughly in proportion to input frequency. The three synapses of the pathway thus transform presynaptic rate in three different ways: depression at EC–DG synapses largely discards it, facilitation at mossy-fiber synapses amplifies it, and the balanced dynamics of Schaffer collateral synapses preserve it. CA1 output thus encodes presynaptic rate at low frequencies, and both rate and recruitment at high frequencies, consistent with its role as the principal output stage of the hippocampal formation[6,8]. Remarkably, this is achieved with only a few Schaffer collateral synapses, although each CA1 pyramidal neuron receives thousands of excitatory inputs[14,44]. Hippocampal output can therefore be controlled by small, selective subsets of CA3 afferents while preserving a large dynamic range for encoding information transmitted through the trisynaptic circuit.

Table 2. Number of synaptic contacts, at nominal peak conductance, able to elicit at least one action potential with 10-90% probability following a single synchronous activation. The pre–post ratio indicates the approximate number of corresponding presynaptic neurons represented by the synapses.

Postsynaptic neuron	Nr. of synapses	Approx. pre:post ratio
DG	5–13	2–7:1
CA3	63-68	∼ 2 : 1
CA1	2–8	1–4:1

3.2 Population recordings indicate the synaptic input received by single neurons

To relate the model to in vivo data, we compared the simulated activation curves with the input–output relations measured by Bartesaghi et al.[16] in the guinea pig entorhinal–dentate–hippocampal system. In those experiments, the population spike (PS) evoked in each subregion was measured as a function of the PS in the preceding one. Each transfer followed a sigmoidal

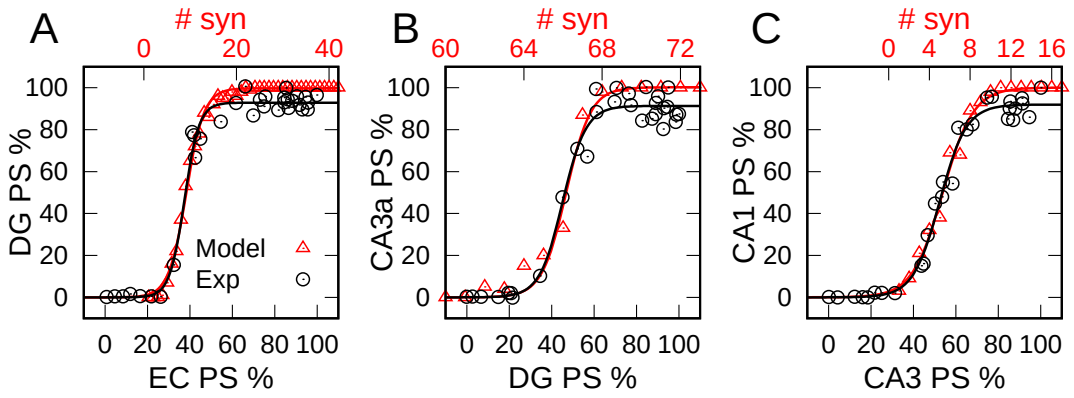


Figure 9. Postsynaptic activation probability for each stage of the trisynaptic circuit. Each panel reports the probability of generating a postsynaptic spike as a function of the presynaptic population spike percentage measured experimentally by Bartesaghi et al.[16] (lower x-axis, black circles) and the number of synaptic contacts used in the simulations (upper x-axis, red triangles). In the model, spike probabilities were computed from 100 trials with random synaptic placement for each condition. Sigmoidal fits (Eq. 1; Supplementary Table ST1) were applied to both data sets, and the upper axis was aligned at the midpoints of the two fits.

relationship with a region-specific threshold and gain. Both the experimental data and the simulated activation curves at the nominal peak conductance (Figs. 3A, 5A, and 7A) were fitted with the sigmoidal function

$$f(x) = \frac{a}{1 + e^{b(c^* - x)}}, \tag{1}$$

where x is the presynaptic PS percentage for the experimental data and the number of synchronously activated synapses for the simulations. The fit parameters are reported in Supplementary Table ST1.

The two fitted curves were related through their postsynaptic activation levels. For a given level y of postsynaptic activation, inverting Eq. 1,

$$x(y) = c^* - \frac{1}{b} \ln\left(\frac{a}{y} - 1\right), \tag{2}$$

gives the presynaptic PS at which this level is reached experimentally (from the experimental fit) and the number of synchronously activated synapses required to reach it on a single neuron (from the model fit). Because the two curves were fitted independently and both are sigmoidal, their agreement in Fig. 9 should not be read as a validation in itself. Their correspondence, however, provides a quantitative estimate of how much synchronous input a single neuron receives at a given level of presynaptic population activity. We evaluated it at the onset of the postsynaptic response (10% postsynaptic PS) and near its saturation (90% postsynaptic PS) (Table 3). The slope factor of the model fit, b_{Model}, determines how many additional synapses are needed to cover this range, $\ln 81 / b_{\mathrm{Model}}$.

Table 3. Synchronous input to a single postsynaptic neuron at the onset (10%) and near the saturation (90%) of the postsynaptic population response. For each level, the experimental fit gives the corresponding presynaptic PS and the model fit gives the number of synchronously activated synapses (Eq. 2; parameters in Supplementary Table ST1). For DG-CA3, ranges span the adapting, bursting, and non-adapting CA3 phenotypes. The last three columns refer to 90% postsynaptic PS.

Stage	Syn gained from 10% to 90% ($\ln 81/b_{\mathrm{Model}}$)	syn at 10% activation	syn at 90% activation	Equivalent presynaptic neurons at 90% PS	Fraction of anatomical convergence
EC→DG	∼8.5	∼5 (∼30% EC PS)	∼13 (∼49% EC PS)	∼7 EC neurons	∼0.16%
DG→CA3	∼2.1-3.3	∼63-65 (∼34% DG PS)	∼65-68 (∼69% DG PS)	∼2 granule cells	∼4%
CA3→CA1	∼6.6	∼2 (∼39% CA3 PS)	∼9 (∼76% CA3 PS)	∼4 CA3 neurons	∼0.07%

The three stages differ markedly. In DG, the postsynaptic response began (10%) at ∼30% EC PS, when a granule cell received ∼5 synchronous perforant-path synapses, and approached saturation (90%) at ∼49% EC PS, with ∼13 synapses. The

rise in EC population activity over this range thus corresponds to only ∼8 additional synapses per granule cell. In CA3 the postsynaptic response began at ∼34% DG PS, with ∼63-65 mossy-fiber synapses depending on the firing phenotype (Table 3), and reached 90% at ∼69% DG PS, with ∼65-68 synapses. A 35-point increase in the activity of the granule cell population therefore corresponds to only ∼2-3 additional mossy-fiber synapses per CA3 neuron, less than a tenth of the contacts made by a single granule cell. The steep population-level transition observed experimentally thus reflects a very small increment of mossy-fiber input onto each neuron. In CA1, the postsynaptic response began at ∼39% CA3 PS, with ∼2 Schaffer collateral synapses, and reached 90% at ∼76% CA3 PS, with ∼9 synapses. At all three stages, even near-saturating population responses correspond to only a small fraction of the anatomical convergence onto each neuron, from ∼0.07% in CA1 to ∼4% in CA3. This further supports the conclusion that only a small subset of anatomical connectivity participates in the transmission of a given signal.

Matching two independently fitted sigmoids also has limits, which define what the comparison can test. First, the correspondence is meaningful only if both relations are well described by the same functional form. A simulated activation curve that was non-monotonic, or markedly asymmetric between the foot and the shoulder of the transition, would not be captured by Eq. 1. Second, the postsynaptic axis is not rescaled. A model that failed to reach full activation, for example because of depolarization block, could not reproduce the experimental saturation. The fitted saturation levels were in fact similar: ∼92% for the experimental data, reflecting their normalization and scatter, and ∼100% for the model (Supplementary Table ST1). Third, the synaptic input delivered by a given level of presynaptic activity depends on the presynaptic population, not on the properties of the postsynaptic neuron. Postsynaptic variants receiving the same input should therefore require similar numbers of synapses at the same presynaptic PS. This was the case for the three CA3 firing phenotypes, whose activation thresholds all fell within ∼63–68 mossy-fiber synapses and which all reproduced the experimental relationship (Fig. 9B; Supplementary Fig. S6). The transfer function at this stage is therefore set by mossy-fiber convergence rather than by intrinsic firing properties.

3.3 A few synapses shape single-neuron computation

Fig. 10 summarizes the transformations performed by single neurons at each stage of the circuit. For a single synchronous volley at the physiological conductance, the transition from 10% to 90% firing probability required 5–13 perforant-path synapses on a granule cell (2–7 EC neurons), 63–68 mossy-fiber contacts on a CA3 pyramidal cell (∼2 granule cells), and 2–8 Schaffer collateral synapses on a CA1 pyramidal cell (1–4 CA3 neurons). At half-activation, these numbers correspond to ∼0.1%, ∼4%, and ∼0.05% of the anatomical convergence onto each cell type. The three stages differ in how unitary inputs combine (sublinearly, linearly, and supralinearly), in how short-term synaptic dynamics transform input rate (discarded, amplified, or preserved), and in their output (saturating, bursting, or about one spike per input event). Granule cells thus count co-active inputs, CA3 neurons gate on one or two specific granule cells, and CA1 neurons relay both the rate and the recruitment of their CA3 afferents.

The small number of inputs required has direct consequences for the computational properties of individual neurons. If k co-active presynaptic neurons suffice to drive a cell receiving input from N neurons, the number of distinct groups able to drive it is very large: $\sim 10^{15}$ groups of 5 EC neurons for a granule cell, and $\sim 10^{10}$ groups of 3 CA3 neurons for a CA1 cell. Most of these groups share inputs with many others, so a more meaningful measure is the number of groups that overlap too little for the partial activation of one to substitute for another. Groups sharing at most one presynaptic neuron still number $\sim 10^{5}$–10^{6} for both cell types. Even completely disjoint groups number ∼700 for a granule cell and ∼1,800 for a CA1 cell. Each neuron can therefore act as a reader for a very large number of small, largely independent assemblies. CA3 is the exception. With ∼46 granule cells converging onto each pyramidal neuron[14] and two of them sufficient for activation, its mossy-fiber input supports only ∼1,000 possible granule cell pairs, of which ∼20 are disjoint. Selection at this stage is set by the identity of very few granule cells, and the combinatorial richness of CA3 representations must arise from its recurrent collaterals, which are not included here.

A low threshold also means that modifying the strength of a handful of contacts can move a neuron across threshold for a given input pattern. How effectively such changes act depends on the summation regime. In CA1, where summation is supralinear, doubling the Schaffer collateral conductance reduced the half-activation requirement from ∼5 to ∼2 synapses, the input from a single CA3 neuron (Fig. 7A). Potentiating the contacts made by one presynaptic neuron could therefore be sufficient to make a CA1 pyramidal cell responsive to it. The same property makes neurons sensitive to chance coincidences among their thousands of afferents. Selective responses therefore require that background coincident activity remains low or is suppressed, most likely by inhibition and background synaptic activity, which were not included in the present simulations. The numbers reported here should accordingly be regarded as estimates of the minimal recruitment under favorable conditions.

4 Discussion

We used biophysically detailed models of the principal neurons of the trisynaptic circuit, with experimentally constrained synaptic multiplicity, strength, location, and short-term dynamics, to estimate how many co-active inputs are needed to drive each neuron. The central result is that the requirement is very small at every stage. A single synchronous volley activates a granule cell with 5–13 perforant-path synapses (2–7 EC neurons), a CA3 pyramidal cell with 63–68 mossy-fiber contacts (~ 2 granule cells, or one firing repetitively), and a CA1 pyramidal cell with 2–8 Schaffer collateral synapses (1–4 CA3 neurons). These numbers correspond to ~ 0.05–4% of the anatomical convergence onto each cell type (Fig. 10). They are also well below the tens to hundreds of co-active neurons often assumed to be needed to discharge a downstream "reader" neuron. Our results suggest that in the hippocampus, functional assemblies capable of driving a target neuron can be much smaller than generally assumed, down to a single presynaptic neuron in the case of repetitively active granule cells, and to a few neurons in CA1.

Beyond the numbers, the three stages differ in two properties that determine how input is converted into output. The first is how unitary inputs combine. Summation was sublinear in granule cells, approximately linear for proximal mossy-fiber inputs in CA3, and supralinear in CA1, where a few strong inputs were more effective than many weak ones. The second is how input rate is transformed by short-term synaptic dynamics. Depression at perforant-path synapses made granule cell output largely independent of afferent firing rate above $\sim$ 20–30 Hz. Facilitation at mossy-fiber synapses made CA3 highly sensitive to the firing rate of individual granule cells. The balance of facilitation and depression at Schaffer collateral synapses made the drive per contact increase approximately in proportion to input frequency, so that CA1 neurons fired about one spike per input event over a wide range of frequencies. Each stage therefore reads a different feature of its input. Granule cells respond mainly to how many afferents are co-active. CA3 neurons respond to the identity and spike count of one or two specific granule cells. CA1 neurons respond to both the number and the rate of their active CA3 afferents. In this view, the sequential transformations along the circuit arise from the combination of synaptic dynamics and dendritic integration at each stage, rather than from intrinsic excitability alone.

These conclusions are consistent with experimental observations at the extremes of the pathway. Single granule cells can discharge their CA3 targets *in vivo* when firing in bursts[18], as predicted here by the combination of mossy-fiber facilitation and the ~ 37 contacts made by each granule cell. More broadly, stimulation of single cortical neurons can influence behavior[55], and holographic activation of a few neurons can recall entire cortical ensembles[56]. This indicates that very small groups of neurons can have measurable downstream effects. Our results provide a cellular-level explanation for how this may occur in the hippocampus. The comparison with population recordings[16] adds a complementary constraint: the mapping between population spike amplitude and synaptic input predicts that even near-saturating postsynaptic population responses correspond to synchronous input from only $\sim$0.07–4% of the anatomical synapses onto each neuron (Table 3).

The model makes several predictions that can be tested experimentally. First, synchronous activation of 2–4 identified CA3 neurons, for example by two-photon holographic optogenetics, should be sufficient to discharge a connected CA1 pyramidal cell. Second, the frequency insensitivity of granule cell output should depend on short-term depression at perforant-path synapses and should be reduced by blocking the presynaptic mechanisms of perforant-path depression. Third, the ability of a single repetitively firing granule cell to drive CA3 should be lost when mossy-fiber facilitation is reduced. Finally, the supralinear summation predicted in CA1 implies that potentiation of the contacts made by a single CA3 neuron should be sufficient to make a CA1 pyramidal cell reliably responsive to it.

The estimates were obtained under simplifying conditions, and their limitations should be considered. Transmission was analyzed between single presynaptic–postsynaptic pairs, with perfectly synchronous activation, deterministic release, uniformly random synaptic placement within each dendritic region, and a single morphology per cell type. Inhibition, neuromodulation, and background synaptic activity were not included. Temporal jitter, release failures, and feedforward inhibition would all increase the number of inputs required. Conversely, the background depolarization and neuromodulatory states present *in vivo* could decrease it. In addition, the short-term plasticity parameters were derived from *in vitro* recordings, and the population data used for comparison were obtained in guinea pig, whereas the cell models are based on rat data. None of these factors is likely to bridge the one to three orders of magnitude separating the estimated requirements from the anatomical convergence. They do, however, imply that the specific numbers should be read as estimates of the minimal recruitment under favorable conditions rather than as exact biological values.

These results provide quantitative constraints for network models of the hippocampus. Large-scale simulations commonly rely on probabilistic connectivity and averaged convergence values. Without constraints on the minimal recruitment needed for propagation, such models may operate in regimes of synaptic convergence that are far from physiological. The thresholds, summation regimes, and short-term dynamics characterized here offer biologically grounded boundary conditions for such models. They also suggest that network models should reproduce not only firing rates and oscillatory dynamics but also the small size of the effective assemblies that drive individual neurons. Extending the present framework to include inhibitory circuits, stochastic release, and network-level interactions will be essential to determine how these single-neuron properties shape hippocampal dynamics during learning, memory formation, and retrieval, and how they contribute to circuit vulnerability

Transformations along the hippocampal trisynaptic circuit

	Perforant path (depressing)	*Mossy fibers (facilitating)*	*Schaffer collaterals (facilitating + depressing)*
Entorhinal cortex →	**Dentate gyrus**	**CA3**	**CA1**
Synapses for 10–90% activation (single volley)	5–13	63–68	2–8
Presynaptic neurons	2–7 EC neurons	~2 granule cells	1–4 CA3 neurons
Fraction of anatomical input for 50% spike prob.	~0.1%	~4%	~0.05%
Summation of unitary inputs	Sublinear	Linear	Supralinear
Effect of input rate (STP)	Discarded	Amplified	Preserved
Output	Saturates (~18 Hz)	Bursts; declines with excess drive	~1 spike per input event
Operation	**Counts co-active inputs**	**Gates on 1–2 granule cells**	**Relays rate and recruitment**

Figure 10. Summary of the single-neuron transformations along the trisynaptic circuit derived from the simulations. Synapse numbers refer to the 10–90% activation range for a single synchronous volley at physiological conductance; presynaptic neuron numbers assume the synapses per connection in Table 1. Fraction of anatomical input was calculated for 50% spike probability.

in pathological conditions.

Funding.

The authors acknowledge a contribution from the Italian National Recovery and Resilience Plan (NRRP), funded by the European Union – NextGenerationEU (Project IR0000011, CUP B51E22000150006, 'EBRAINS-Italy', and Project PRIN 2022ZY5RXB_002 'HIPPOCOMP'), the EU Horizon Europe Programme under the Specific Grant Agreement No. 101147319 (EBRAINS 2.0 Project), the Grant No. PID2023-147734NB-I00 funded by the Spanish MCIN/AEI/10.13039/501100011033 and the support of the Aragon Government to the Recognized group 'E36_26R Física Estadística y no-lineal (FENOL)'. We also thank Alessia Bonafede for administrative and technical assistance.

Author contributions statement

RM and MM generated the project. RM wrote the NEURON code. PA performed the preliminary simulations and summarized the outcomes. AF, RM, MM analyzed the results and derived the conclusions. All authors revised the manuscript.

Competing Interests

The authors declare no potential conflict of interests.

Data Availability

Model and simulation files are available for download on modelDB (https://modeldb.science/ acc.n. 2041699). The read-only access code for review purposes only is 20261020.

References

1. Liu X, Ramirez S, Pang PT, Puryear CB, Govindarajan A, Deisseroth K, & Tonegawa S. Optogenetic stimulation of a hippocampal engram activates fear memory recall. *Nature* 2012;484(7394):381–385. doi: 10.1038/nature11028.
2. Morris AM, Churchwell JC, Kesner RP, & Gilbert PE. Selective lesions of the dentate gyrus produce disruptions in place learning for adjacent spatial locations. *Neurobiology of learning and memory* 2012;97(3):326–331. doi: 10.1016/j.nlm.2012.02.005.
3. O'Keefe J, & Dostrovsky J. The hippocampus as a spatial map. Preliminary evidence from unit activity in the freely moving rat. *Brain research* 1971;34(1):171–175. doi: 10.1016/0006-8993(71)90358-1.
4. Scoville WB, & Milner B. Loss of recent memory after bilateral hippocampal lesions. *Journal of neurology, neurosurgery, and psychiatry* 1957;20(1):11–21. doi: 10.1136/jnnp.20.1.11.
5. Stupien G, Florian C, & Roullet P. Involvement of the hippocampal CA3-region in acquisition and in memory consolidation of spatial but not in object information in mice. *Neurobiology of learning and memory* 2003;80(1):32–41. doi: 10.1016/s1074-7427(03)00022-4.
6. Amaral DG, & Witter MP. The three-dimensional organization of the hippocampal formation: a review of anatomical data. *Neuroscience* 1989;31(3):571–591. doi: 10.1016/0306-4522(89)90424-7.
7. Naber PA, Witter MP, & Lopes Silva FH. Networks of the hippocampal memory system of the rat. The pivotal role of the subiculum. *Annals of the New York Academy of Sciences* 2000;911:392–403. doi: 10.1111/j.1749-6632.2000.tb06739.x.
8. Witter MP. Connectivity of the Hippocampus. In: Cutsuridis, Vassilis & Graham, Bruce & Cobb, Stuart & Vida, Imre. *Hippocampal Microcircuits a Computational Modeler's Resource Book*:5-26. New York, NY: Springer 2010.
9. Stepan J, Dine J, & Eder M. Functional optical probing of the hippocampal trisynaptic circuit in vitro: network dynamics, filter properties, and polysynaptic induction of CA1 LTP. *Frontiers in neuroscience* 2015;9:160. doi: 10.3389/fnins.2015.00160.
10. Stepan J, Dine J, Fenzl T, Polta SA, von Wolff G, Wotjak CT, & Eder M. Entorhinal theta-frequency input to the dentate gyrus trisynaptically evokes hippocampal CA1 LTP. *Frontiers in neural circuits* 2012;6:64. doi: 10.3389/fncir.2012.00064.
11. Winson J. Loss of hippocampal theta rhythm results in spatial memory deficit in the rat. *Science (New York, N.Y.)* 1978;201(4351):160–163. doi: 10.1126/science.663646.
12. Buzsáki G, & Moser EI. Memory, navigation and theta rhythm in the hippocampal–entorhinal system. *Nature neuroscience* 2013;16(2):130–138. doi: 10.1038/nn.3304.

13. Fernández-Ruiz A, Oliva A, Soula M, Rocha-Almeida F, Nagy GA, Martin-Vazquez G, & Buzsáki G. Gamma rhythm communication between entorhinal cortex and dentate gyrus neuronal assemblies. *Science (New York, N.Y.)* 2021;372(6537):eabf3119. doi: 10.1126/science.abf3119.

14. Amaral DG, Ishizuka N, & Claiborne B. Neurons, numbers, and the hippocampal network. *Progress in brain research* 1990;83:1–11. doi: 10.1016/s0079-6123(08)61237-6.

15. Megías M, Emri Z, Freund TF, Gulyás AI. Total number and distribution of inhibitory and excitatory synapses on hippocampal CA1 pyramidal cells. *Neuroscience.* 2001;102(3):527-40. doi: 10.1016/s0306-4522(00)00496-6.

16. Bartesaghi R, Migliore M, & Gessi T. Input-output relations in the entorhinal cortex-dentate-hippocampal system: evidence for a non-linear transfer of signals. *Neuroscience* 2006;142(1):247–265. doi: 10.1016/j.neuroscience.2006.06.001.

17. Jonas P, Major G, & Sakmann B. Quantal components of unitary EPSCs at the mossy fibre synapse on CA3 pyramidal cells of rat hippocampus. *The Journal of physiology* 1993;472:615–663. doi: 10.1113/jphysiol.1993.sp019965.

18. Henze DA, Wittner L, & Buzsáki G. Single granule cells reliably discharge targets in the hippocampal CA3 network in vivo. *Nature neuroscience* 2002;5(8):790–795. doi: 10.1038/nn890.

19. Häusser M, Mel B. Dendrites: bug or feature? *Curr Opin Neurobiol.* 2003;13(3):372–383. doi: 10.1016/s0959-4388(03)00075-8.

20. London M & Häusser M. Dendritic computation. *Annu Rev Neurosci.* 2005;28:503–532. doi: 10.1146/annurev.neuro.28.061604.135703.

21. Gasparini S, Migliore M & Magee JC. On the Initiation and Propagation of Dendritic Spikes in CA1 Pyramidal Neurons. *The Journal of Neuroscience* 2004;24(49):11046–11056. doi: 10.1523/JNEUROSCI.2520-04.2004

22. Losonczy A, Magee JC. Integrative properties of radial oblique dendrites in hippocampal CA1 pyramidal neurons. *Neuron* 2006;50(2):291-307. doi: 10.1016/j.neuron.2006.03.016.

23. Poirazi P, Brannon T, Mel BW. Pyramidal neuron as two-layer neural network. *Neuron* 2003;37(6):989-999. doi: 10.1016/s0896-6273(03)00149-1.

24. Beniaguev D, Segev I, London M. Single cortical neurons as deep artificial neural networks. *Neuron* 2021;109(17):2727-2739. doi: 10.1016/j.neuron.2021.07.002.

25. Buzsáki G. Neural syntax: cell assemblies, synapsembles, and readers. *Neuron* 2010;68(3):362-85. doi: 10.1016/j.neuron.2010.09.023.

26. Harris KD, Csicsvari J, Hirase H, Dragoi G, Buzsáki G. Organization of cell assemblies in the hippocampus. *Nature* 2003;424(6948):552-6. doi: 10.1038/nature01834.

27. Hines ML, Carnevale NT. The NEURON simulation environment. *Neural Comput.* 1997;9:1179.

28. Ferrante M, Migliore M, & Ascoli GA. Feed-forward inhibition as a buffer of the neuronal input-output relation. *Proceedings of the National Academy of Sciences of the United States of America* 2009;106(42):18004–18009. doi: 10.1073/pnas.0904784106.

29. Martinello K, Huang Z, Lujan R, Tran B, Watanabe M, Cooper EC, Brown DA & Shah MM. Cholinergic Afferent Stimulation Induces Axonal Function Plasticity in Adult Hippocampal Granule Cells. *Neuron.* 2015;85(2):346-363. doi: 10.1016/j.neuron.2014.12.030.

30. Gao TM, Howard EM, & Xu ZC. (1998). Transient neurophysiological changes in CA3 neurons and dentate granule cells after severe forebrain ischemia in vivo. Journal of neurophysiology, 80(6), 2860–2869. doi: 10.1152/jn.1998.80.6.2860.

31. Scharfman HE. Electrophysiological diversity of pyramidal-shaped neurons at the granule cell layer/hilus border of the rat dentate gyrus recorded in vitro. *Hippocampus* 1995;5(4):287–305. doi: 10.1002/hipo.450050403.

32. Yun SH, Gamkrelidze G, Stine WB, Sullivan PM, Pasternak JF, Ladu MJ, & Trommer BL. Amyloid-beta1-42 reduces neuronal excitability in mouse dentate gyrus. *Neuroscience letters* 2006;403(1-2):162–165. doi: 10.1016/j.neulet.2006.04.065.

33. Hemond P, Epstein D, Boley A, Migliore M, Ascoli GA & Jaffe DB. Distinct classes of pyramidal cells exhibit mutually exclusive firing patterns in hippocampal area CA3b. *Hippocampus* 2008;18(4):411–424. doi: 10.1002/hipo.20404.

34. Migliore M, De Simone G, & Migliore R. Effect of the initial synaptic state on the probability to induce long-term potentiation and depression. *Biophysical journal* 2015;108(5):1038–1046. doi: 10.1016/j.bpj.2014.12.048.

35. Migliore M, Hoffman, DA, Magee JC, & Johnston D. Role of an A-type K+ conductance in the backpropagation of action potentials in the dendrites of hippocampal pyramidal neurons. *Journal of computational neuroscience* 1999;7(1):5–15. doi: 10.1023/a:1008906225285.

36. Migliore M, Cook EP, Jaffe DB, Turner DA, & Johnston D. Computer simulations of morphologically reconstructed CA3 hippocampal neurons. *Journal of neurophysiology* 1995;73(3):1157–1168. doi: 10.1152/jn.1995.73.3.1157.

37. Migliore M. On the integration of subthreshold inputs from Perforant Path and Schaffer Collaterals in hippocampal CA1 pyramidal neurons. *Journal of computational neuroscience* 2003;14(2):185–192. doi: 10.1023/a:1021906818333.

38. Migliore R, Lupascu CA, Bologna LL, Romani A, Courcol JD, Antonel S, Van Geit WAH, Thomson AM, Mercer A, Lange S, Falck J, Rössert CA, Shi Y, Hagens O, Pezzoli M, Freund TF, Kali S, Muller EB, Schürmann F, Markram H, Migliore M. The physiological variability of channel density in hippocampal CA1 pyramidal cells and interneurons explored using a unified data-driven modeling workflow. *PLoS computational biology* 2018;14(9):e1006423. doi: 10.1371/journal.pcbi.1006423.

39. Sáray S, Rössert CA, Appukuttan S, Migliore R, Vitale P, Lupascu CA, Bologna LL, Van Geit W, Romani A, Davison AP, Muller E, Freund TF, & Káli S. HippoUnit: A software tool for the automated testing and systematic comparison of detailed models of hippocampal neurons based on electrophysiological data. *PLoS computational biology* 2021;17(1):e1008114. doi: 10.1371/journal.pcbi.1008114.

40. Steward O, & Scoville SA. Cells of origin of entorhinal cortical afferents to the hippocampus and fascia dentata of the rat. *The Journal of comparative neurology* 1976;169(3):347–370. doi: 10.1002/cne.901690306.

41. Dyhrfjeld-Johnsen J, Santhakumar V, Morgan RJ, Huerta R, Tsimring L, & Soltesz I. Topological determinants of epileptogenesis in large-scale structural and functional models of the dentate gyrus derived from experimental data. *Journal of neurophysiology* 2007;97(2):1566–1587. doi: 10.1152/jn.00950.2006.

42. Santhakumar V, Bender R, Frotscher M, Ross ST, Hollrigel GS*, Toth Z & Soltesz I. Granule cell hyperexcitability in the early post-traumatic rat dentate gyrus: the "irritable mossy cell" hypothesis. *Journal of Physiology* 2000;524.1:117-134. doi: 10.1111/j.1469-7793.2000.00117.x

43. Forti L, Bossi M, Bergamaschi A, Villa A, & Malgaroli A. Loose-patch recordings of single quanta at individual hippocampal synapses. *Nature* 1997;388(6645):874–878. doi: 10.1038/42251.

44. Bezaire MJ, & Soltesz I. Quantitative assessment of CA1 local circuits: knowledge base for interneuron-pyramidal cell connectivity. *Hippocampus* 2013;23(9):751–785. doi: 10.1002/hipo.22141.

45. Abbott LF, Varela JA, Sen K, Nelson SB. Synaptic depression and cortical gain control. *Science* 1997;275(5297):220-4. doi: 10.1126/science.275.5297.221.

46. Tsodyks MV, Markram H. The neural code between neocortical pyramidal neurons depends on neurotransmitter release probability. *Proc Natl Acad Sci* USA 1997;94(2):719-23. doi: 10.1073/pnas.94.2.719.

47. Treves A, & Rolls ET. Computational analysis of the role of the hippocampus in memory. *Hippocampus* 1994;4(3):374–391. doi: 10.1002/hipo.450040319.

48. Hsu D. The dentate gyrus as a filter or gate: a look back and a look ahead. *Progress in brain research* 2007;163:601–613. doi: 10.1016/S0079-6123(07)63032-5.

49. McHugh TJ, Jones MW, Quinn JJ, Balthasar N, Coppari R, Elmquist JK, Lowell BB, Fanselow MS, Wilson MA, & Tonegawa S. Dentate gyrus NMDA receptors mediate rapid pattern separation in the hippocampal network. *Science (New York, N.Y.)* 2007;317(5834):94–99. doi: 10.1126/science.1140263.

50. Knierim JJ, & Neunuebel JP. Tracking the flow of hippocampal computation: Pattern separation, pattern completion, and attractor dynamics. *Neurobiology of learning and memory* 2016;129:38–49. doi: 10.1016/j.nlm.2015.10.008.

51. McNaughton, B. L., & Morris, R. G. Hippocampal synaptic enhancement and information storage within a distributed memory system. *Trends in neurosciences* 1987;10:408–415. doi: 10.1016/0166-2236(87)90011-7.

52. Rolls, E. T. The mechanisms for pattern completion and pattern separation in the hippocampus. *Frontiers in systems neuroscience* 2013;7:74. doi: 10.3389/fnsys.2013.00074.

53. Salin PA, Scanziani M, Malenka RC, Nicoll RA. Distinct short-term plasticity at two excitatory synapses in the hippocampus. *Proc Natl Acad Sci* USA 1996;93(23):13304-9. doi: 10.1073/pnas.93.23.13304.

54. Nicoll RA, Schmitz D. Synaptic plasticity at hippocampal mossy fibre synapses. *Nat Rev Neurosci* 2005;6(11):863-76. doi: 10.1038/nrn1786.

55. Houweling AR, Brecht M. Behavioural report of single neuron stimulation in somatosensory cortex. *Nature* 2008;451(7174):65-8. doi: 10.1038/nature06447.

56. Carrillo-Reid L, Han S, Yang W, Akrouh A, Yuste R. Controlling Visually Guided Behavior by Holographic Recalling of Cortical Ensembles. *Cell* 2019;178(2):447-457.e5. doi: 10.1016/j.cell.2019.05.045.

Supplementary Files

This is a list of supplementary files associated with this preprint. Click to download.

- HTCSRSM.pdf